

Numerical Optimization of Proton Exchange Membrane Fuel Cell Cathodes

M. Secanell^a, B.Carnes^b, A. Suleman^a and N.Djilali^{a,*}

^a*Institute for Integrated Energy Systems and Dept. Mechanical Engineering,
University of Victoria, PO Box 3055 STN CSC, Victoria, BC, V8W 3P6*

^b*Sandia National Laboratories, P.O. Box 5800, Albuquerque, NM 87185-0382*

Abstract

A fuel cell gradient-based optimization framework based on adaptive mesh refinement and analytical sensitivities is presented. The proposed approach allows for efficient and reliable multivariable optimization of fuel cell designs. A two-dimensional single-phase cathode electrode model that accounts for voltage losses across the electrolyte and solid phases and water and oxygen concentrations is implemented using an adaptive finite element formulation. Using this model, a multivariable optimization problem is formulated in order to maximize the current density at a given electrode voltage with respect to electrode composition parameters and the optimization problem is solved using a gradient-based optimization algorithm. In order to solve the optimization problem effectively using gradient-based optimization algorithms, the analytical sensitivity equations of the model with respect to the design variables are obtained. This approach reduces the necessary computational time to obtain the gradients and improves significantly their accuracy when compared to gradients obtained using numerical sensitivities. Optimization results show a substantial increase in the fuel cell performance achieved by increasing platinum loading and reaching a Nafion mass fraction around 20-30%wt. in the catalyst layer.

Key words: PEM fuel cell, catalyst layer, sensitivity analysis, optimization, finite elements

1 Introduction

The design of proton exchange membrane fuel cells (PEMFCs) involves trade-offs which can be difficult to quantify and balance due to the coupling of a large number of complex transport phenomena. These phenomena, which include fluid flow, heat and charge transport, and electrochemistry [1], are controlled by a large number of variable parameters such as material properties, sizing of components and operating conditions. Numerical models can provide valuable insight on the effect of these parameter variations on performance [2–5] which are difficult to predict and often result in opposing effects. For instance, increasing the size of the cathode gas distribution channel can alleviate mass transport limitations but this is offset by increased ohmic losses [6], and the optimal size is in fact dependent on properties such as gas diffusion layer porosity, permeability and conductivity. Optimal design requires therefore simultaneous variation of all pertinent design parameters.

When only one or two design parameters are involved, optimization can be achieved using parametric studies and graphical techniques. However, when the number of design parameters increases, these techniques are not feasible and numerical optimization methodologies are required. Numerical methods for large scale optimal design, involving optimization of a large number of

* Corresponding author.

Email addresses: `secanell@uvic.ca` (M. Secanell), `ndjilali@uvic.ca` (N.Djilali).

design variables, have been developed in other areas such as aerospace [7–9], structural and engineering design [10,11]. These methods rely on analytical sensitivity computations and gradient-based optimization algorithms. Optimization studies in some areas of fuel cell design have started to appear in recent years [12–16]. However, these methods are limited to optimization problems with a small number of design variables because the models used do not provide sufficiently accurate sensitivities and the procedures were based on either numerical sensitivities [13–15] or zero-order search methods which rely excessively on computationally resources [12,16]. In this paper, a method to obtain analytical sensitivities is presented and used to implement a numerical model (programmed in C++) that solves the governing equations of the model as well as the sensitivity equations.

The electrode in a PEMFC is a critical component from the view point of both cost and performance and is therefore a good candidate for optimization. In order to reduce fuel cell costs, the amount of platinum used in the catalyst layers and, in particular, in the cathode catalyst layer, has to be minimized and distributed effectively while maximizing the power density. With the exception of the recent work by Song et al. [17,18] where a one-dimensional catalyst layer model was used in conjunction with numerical optimization, most of the experimental or modeling work to date to optimize catalyst layer and electrode compositions has been performed using either single variable trial-and-error or parametric studies in conjunction with graphical methods. These methods are only valid when the number of design parameters is one or two, however, electrode design involves more than two design variables (e.g. Pt loading distribution, porosity and Nafion volume fraction) and therefore, numerical optimization is required to solve such problem.

A multivariable numerical optimization analysis coupled with a two-dimensional cathode electrode model is presented in this paper. The model fully accounts for voltage losses across the electrode and water and oxygen concentration in the catalyst layer and gas diffusion layer, and is implemented using an adaptive finite element formulation. Following a detailed discussion and validation of the model in section 2, a multivariable optimization problem is formulated to maximize the current density for a given electrode overpotential with respect to electrode composition parameters and subject to physical constraints. In order to solve the optimization problem effectively using gradient-based optimization algorithms, the analytical sensitivity equations of the model with respect to gas diffusion layer (GDL) and catalyst layer (CL) design variables are obtained. The optimization problem and the sensitivity equations are discussed in section 3 together with the validation of the analytical sensitivities by comparing the analytical gradients to numerical gradients obtained using forward differences. Finally, the validated model and sensitivities are coupled to a gradient-based optimization algorithm and results are presented and analyzed in section 4.

2 Cathode Electrode Model

In this section, a two-dimensional mathematical model for a cathode electrode representing a plane across the channel of a PEMFC is described. The model is based on the following assumptions:

- The fuel cell operates at steady state and at constant temperature and pressure.
- The cathode is fed by a binary mixture of oxygen and water vapor.

- The gas diffusion layer (GDL) is composed of void space and carbon fibers.
- The catalyst layer (CL) is formed of a mixture of carbon supported platinum, ionomer membrane electrolyte (Nafion) and void space [18,19].
- The transport of reactants from the gas channels to the CL occurs only by diffusion of oxygen gas in water vapor and can be modeled by Fick's first law [2].
- Once the oxygen arrives at the catalyst site, it has to dissolve into an infinitesimally thin layer of ionomer which covers the catalytic sites. This layer is considered infinitesimal because there is no work to date that relates this thickness to the amount of ionomer in the catalyst layer, therefore, it is a simplification needed to pose the optimization problem.
- The transport of protons takes place only through the electrolyte, i.e. the Nafion, and it is governed by Ohm's law.
- The transport of electrons takes place only through the solid phase, i.e. the carbon fibers in the GDL and the mixture of carbon supported platinum in the catalyst layer, and it is governed by Ohm's law.

2.1 Model equations

Using the above assumptions, the equations governing transport in the cathode GDL and CL are written as

$$R(\mathbf{u}, \mathbf{p}) = \begin{cases} \nabla \cdot (nF c_{total} D_{o_2}^{eff} \nabla x_{o_2}) - \nabla \cdot \mathbf{i} = 0 \\ \nabla \cdot (\sigma_m^{eff} \nabla \phi_m) - \nabla \cdot \mathbf{i} = 0 \\ \nabla \cdot (\sigma_S^{eff} \nabla \phi_S) + \nabla \cdot \mathbf{i} = 0 \end{cases} \quad (1)$$

where the unknowns are the oxygen molar fraction x_{o_2} , the ionomer membrane electrical potential ϕ_m and the solid phase electrical potential ϕ_s . These equations are solved for both the GDL and CL domains and, therefore, the system of equations fully coupled these domains. Furthermore, the physical properties of the GDL and CL, oxygen diffusion coefficient, $D_{o_2}^{eff}$, proton conductivity, σ_m^{eff} , and electron conductivity, σ_s^{eff} , are related to the material composition. Similarly, the volumetric current density, $\nabla \cdot \mathbf{i}(x_{o_2}, \phi_m, \phi_s)$, is also dependent on the catalyst layer composition. The appropriate relationships between these coefficients and the cathode composition are described below and are based on the work by Kulikovsky et al. [20], Song et al. [17] and Marr and Li [21].

The effective oxygen diffusion coefficient is computed using the Bruggeman correction [17] to account for the effect of the porosity and conductive path tortuosity and is given by

$$D_{o_2}^{eff-gdl} = D_{o_2,w}(\epsilon_V^{gdl})^{3/2} \quad (2)$$

$$D_{o_2}^{eff-cl} = D_{o_2,w}(\epsilon_V^{cl})^{3/2} \quad (3)$$

where $D_{o_2}^{eff-gdl}$ and $D_{o_2}^{eff-cl}$ are the effective oxygen diffusion coefficients in the GDL and CL respectively. In the GDL, ϵ_V^{gdl} represents the void space volume fraction. This value is related to the GDL solid phase by,

$$\epsilon_V^{gdl} + \epsilon_S^{gdl} = 1 \quad (4)$$

In the CL, ϵ_V^{cl} represents the volume fraction of the catalyst layer occupied by void space, i.e. the catalyst layer porosity. This value is related to the ionomer volume fraction, ϵ_N^{cl} , i.e. the volume of catalyst layer occupied by the polymer electrolyte (typically Nafion), and the solid phase volume fraction in

the catalyst layer, ϵ_S^{cl} , by the equation

$$\epsilon_N^{cl} + \epsilon_V^{cl} + \epsilon_S^{cl} = 1 \quad (5)$$

where the solid phase volume fraction in the catalyst layer is assumed to be the volume fraction of the catalyst layer occupied by the carbon supporting particles and catalyst particles. The volume fraction of the solid phase can be obtained using [17,21]

$$\epsilon_S^{cl} = \left(\frac{1}{\rho_{Pt}} + \frac{1 - \%Pt}{\%Pt\rho_c} \right) \frac{m_{Pt}}{L} \quad (6)$$

The effective proton and electron conductivities in the catalyst layer, σ_m^{eff} and σ_S^{eff} in (1), are also obtained using Bruggeman correction and are thus

$$\sigma_m^{eff-cl} = \sigma_m^{cl} (\epsilon_N^{cl})^{3/2} \quad (7)$$

$$\sigma_S^{eff-cl} = \sigma_S^{cl} (\epsilon_S^{cl})^{3/2} \quad (8)$$

A similar procedure is used to obtain the effective conductivities in the gas diffusion layer, also known as the porous transport layer. In this layer only solid phase and void space exist and therefore, the effective conductivity of protons and electrons is

$$\sigma_m^{eff-gdl} = \sigma_m^{gdl} (\epsilon_N^{gdl})^{3/2} = 0 \quad (9)$$

$$\sigma_S^{eff-gdl} = \sigma_S^{gdl} (\epsilon_S^{gdl})^{3/2} \quad (10)$$

Note that since the catalyst layer and GDL consist of different materials, the electronic conductivity, σ_S , will also be different in each layer. This change in properties has not been taken into account in most published work.

Finally, the volumetric current density in (1) is also affected by the catalyst layer composition, since either a larger amount of catalytic particles or a larger percentage of platinum per catalyst particle will yield larger volumetric current densities. The volumetric current density is determined using the Tafel equation

$$\nabla \cdot \mathbf{i} = A_v i_0^{ref} \left(\frac{c_{o_2}^{Nafion}}{c_{o_2}^{ref}} \right)^\gamma \exp \left(\frac{\alpha F}{RT} (\phi_m - \phi_s) \right) \quad (11)$$

where $c_{o_2}^{Nafion}$ represents the concentration of oxygen dissolved in Nafion at the catalytic site and is given by

$$c_{o_2}^{Nafion} = \frac{c_{total} x_{o_2}}{H_{o_2,N}} \quad (12)$$

and the dimensionless Henry's law constant is obtained using

$$H_{o_2,N} = \frac{\hat{H}_{o_2,N}}{RT} \quad (13)$$

where $\hat{H}_{o_2,N}$ is taken to be $3.52611 \times 10^4 \frac{Pa \cdot m^3}{mol}$ [22].

The reference exchange current density, i_0^{ref} , in equation (11) is given in A/cm^2 and it is a function of the fuel cell temperature in Kelvin [23]

$$i_0^{ref} = 10^{3.507 - 4001/T} \quad (14)$$

The specific reaction surface area per volume of the catalyst layer, A_v , is dependent on the platinum loading m_{Pt} , the thickness of the catalyst layer L , and the catalyst surface area per unit mass of the catalyst particle, A_0 , [17,21]

$$A_v = A_0 \frac{m_{Pt}}{L} \quad (15)$$

Finally, the catalyst surface area per unit mass of the catalyst particle, A_0 , depends on the platinum content of the catalytic particles. Using a least squares

fit to the data of Marr et al. [21], the following relation is obtained

$$A_0 = 2.2779 \times 10^6 (\%Pt)^3 - 1.5857 \times 10^6 (\%Pt)^2 - 2.0153 \times 10^6 \%Pt + 1.5950 \times 10^6 \quad (16)$$

2.2 Boundary conditions

The two-dimensional model represents a cross-section of the cathode and includes the CL and GDL with appropriate boundary conditions for the membrane-CL, gas channel-GDL and current collector-GDL interfaces. Taking advantage of geometric symmetry, the computation domain includes only half of the gas channel and half of the current collector, as shown in Figure 2.2. There are four types of boundaries

- membrane at $(x, y) = \{x = 0, \forall y\}$;
- symmetric boundaries at $(x, y) = \{\forall x, y = 0 \text{ and } 0.1cm\}$;
- current collector at $(x, y) = \{\forall x, y = [0, 0.05]\}$; and
- gas channel at $(x, y) = \{\forall x, y = [0.05, 0.1]\}$.

The boundary conditions at the membrane/electrode interface (segment A-E in Figure 2.2) are set to [20,22]

$$\mathbf{n} \cdot \nabla x_{o_2} = 0 \quad (17)$$

$$\mathbf{n} \cdot \nabla \phi_S = 0 \quad (18)$$

$$\phi_m = \phi_0 = dV \quad (19)$$

where \mathbf{n} is the surface normal and ϕ_0 , or dV , is the potential across the electrode.

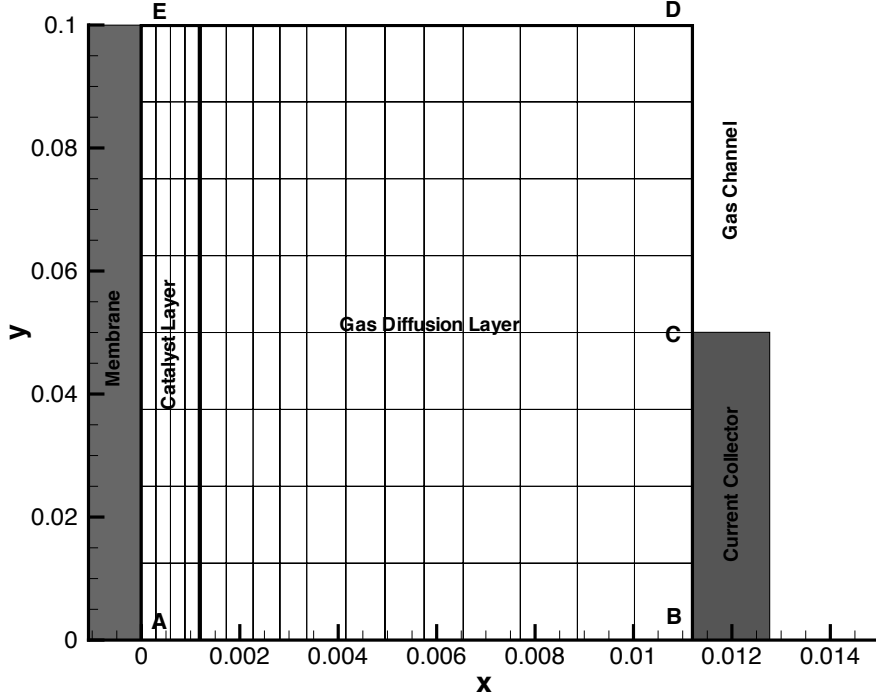


Fig. 1. Computational domain and initial grid used to solve the equations of the cathode electrode model

The boundary conditions along the symmetry boundaries (segments A-B and D-E in Figure 2.2) are set to

$$\mathbf{n} \cdot \nabla x_{o_2} = 0 \quad (20)$$

$$\mathbf{n} \cdot \nabla \phi_S = 0 \quad (21)$$

$$\mathbf{n} \cdot \nabla \phi_m = 0 \quad (22)$$

The boundary conditions at the rib or current collector/electrode interface (segment B-C) reflect the fact that the cathode is taken as the reference po-

tential and are set to

$$\mathbf{n} \cdot \nabla x_{o_2} = 0 \quad (23)$$

$$\phi_S = 0 \quad (24)$$

$$\mathbf{n} \cdot \nabla \phi_m = 0 \quad (25)$$

Finally, the boundary conditions at the gas channel/electrode interface (segment C-D) are set to

$$x_{o_2} = x_{o_2}^0 \quad (26)$$

$$\mathbf{n} \cdot \nabla \phi_S = 0 \quad (27)$$

$$\mathbf{n} \cdot \nabla \phi_m = 0 \quad (28)$$

where the oxygen concentration inside the pores at the GDL/gas channel interface is taken as equal to the concentration of oxygen in the mixture inside the gas channel.

2.3 Numerical validation

The model described in the previous section was discretized using an adaptive finite element method and implemented using C++ and the deal.ii libraries of finite element routines [24]. Note that the solution procedure fully couples the GDL, cathode and sensitivity equations. The implementation of the model and the optimization framework are discussed in detail in section 3.3.

In order to validate the model implementation, the results obtained from the model were compared to the results of Kulikovskiy et al. [20] who presented a similar finite volume model. The main differences between the present model

and that of reference [20] are: a) the use of Fick's first law instead of the Maxwell-Stefan equations, b) the assumption that oxygen has to dissolve in the ionomer before it reacts (in Kulikovsky's model oxygen reacts once it reaches the catalyst site), and finally, c) the dependance of conductivities and diffusion coefficients on electrode composition. The first difference is only nominal since in Kulikovsky et al. [20] results are reported for a fuel cell cathode feed consisting of only oxygen and water vapour. This is a binary mixture, in which case Maxwell-Stefan equation and Fick's first law are equivalent. To eliminate the second difference, in this section we assume that oxygen reacts without having to dissolve into the ionomer, i.e. we set $H_{O_2,N} = 1$. Finally, the input parameters in reference [20] are the effective diffusion coefficients and conductivities rather than the composition of the CL and GDL. To perform a proper comparison, the values reported by Kulikovsky et al. are directly employed in our model to generate the results in this section. These values are given in Table 1. Finally, the conductivity of the ionomer phase was obtained by curve fitting the results by Kulikovsky et al. since a value for this variable was not reported in [20]. In order to validate the model, numerical solutions were obtained to generate polarization curves for two effective electronic conductivities for both GDL and CL, $\sigma_S^{eff} = 0.53 S/cm$ and $\sigma_S^{eff} = 40 S/cm$. For each conductivity, the numerical model was simulated at different overpotentials in order to obtain the current density of the fuel cell. The current density was obtained during postprocessing, as described in detail in Section 3. All solutions were obtained using adaptive refinement. This particular powerful feature of the numerical method ensured grid independent solutions at a minimum computational cost and provides solutions with changes on the current density of less than 1% between the last grid levels. The polarization curves shown in Figure 2 are essentially identical to those of Kulikovsky et al. with

Table 1

Data used to model the catalyst layer [20]

<i>Geometry</i>			
thickness GDL, [cm]	1.0×10^{-2}	thickness cat, [cm]	1.0×10^{-3}
thickness channel, [cm]	0.1	thickness rib, [cm]	0.1
<i>Operating conditions</i>			
p , [atm]	2	T [K]	383
x_{O_2}	0.5	x_{N_2}	0.0
x_w	0.5		
<i>Physical properties</i>			
$D_{O_2}^{eff-gdl}$, [$cm^2 \cdot s^{-1}$]	2.514×10^{-2}	$D_{O_2}^{eff-cl}$, [$cm^2 \cdot s^{-1}$]	6.478×10^{-3}
$H_{O_2,N}$, [$\frac{Pa \cdot m^3}{mol}$]	1		
σ_m^{eff} , [$S \cdot cm^{-1}$]	~ 0.04	σ_S^{eff} , [$S \cdot cm^{-1}$]	0.53-40
α	2	γ	0.5
n	4		
i_0^{ref} , [$A \cdot cm^{-2}$]	1.0×10^5	$c_{O_2}^{ref}$, [$mol \cdot cm^{-3}$]	3.18×10^{-5}
ρ_{Pt} , [$g \cdot cm^{-3}$]	21.5	ρ_c , [$g \cdot cm^{-3}$]	2.0
ρ_N , [$g \cdot cm^{-3}$]	2.0		

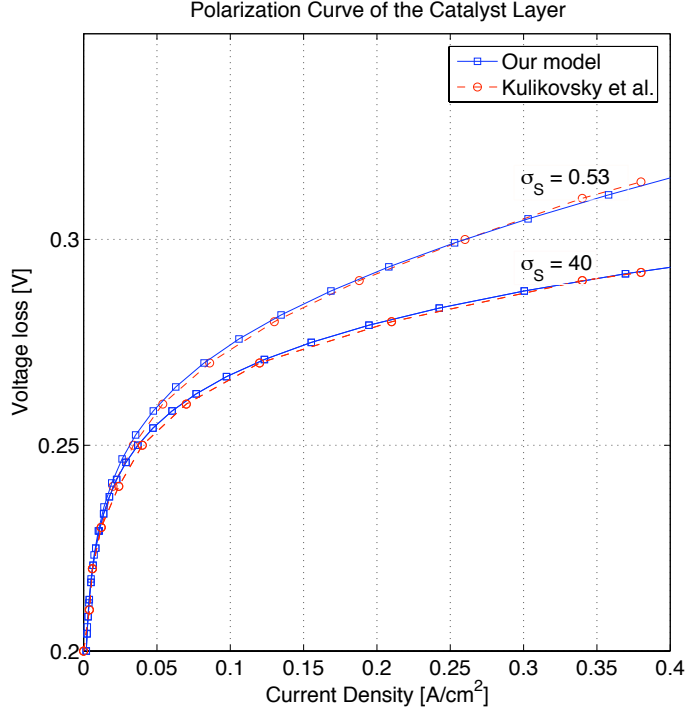


Fig. 2. Comparison between the polarization curves reported in Kulikovsky et al. [20] (circles) and our model's polarization curves (squares)

minor differences likely due to the different numerical technique.

2.4 Input parameters for optimization

The initial input parameters used for optimization are provided in Table 2. These geometric and physical parameters were obtained from either published data or manufacturer's data. The values for the geometry of the electrode are taken from [20,17]. The operating temperature and pressure are similar to other values reported in the literature such as the operating values in [25] and [20]. Similarly, the relative humidity is set to 75% which is also a representative value of a real fuel cell system and similar to the relative humidity values

used by Kulikovsky et al. [20]. This value in conjunction with the saturation pressure curve is used in order to obtain the appropriate molar fractions of oxygen and water.

The physical parameters are also obtained from the literature. The electrolyte conductivity is obtained using the equations provided in [26] for the given temperature and relative humidity. The gas diffusion layer conductivity is obtained assuming a GDL porosity of 80% and an effective resistivity of $40m\Omega \cdot cm$ and by substituting these values into equation (10) to obtain σ_s^{gdl} . The GDL porosity is in the range of the porosity values reported in [27] and for the Toray Carbon Fiber paper. The resistivity values are in the range $6-80m\Omega \cdot cm$ reported for the through-plane and in-plane resistivities for the TGP-H Toray Carbon Fiber paper and in-plane values reported in [27]. It should be noted that the resistivity of the GDL is anisotropic and this should be taken into account in the future. The CL conductivity is obtained by curve fitting the conductivities reported in [28] for Vulcan XC-72 carbon black, commonly used as the carbon supporting the catalyst particles, at different packing values, i.e. the ratio of the volume of the carbon black particles including their micropores and the volume available of the carbon sample. The diffusion coefficient of oxygen in water vapour is obtained from Chapman-Enskog theory as discussed in [29]. The value of Henry's law constant used was reported in [22].

The catalyst layer reaction kinetic parameters, α , γ , n and $c_{o_2}^{ref}$, the initial catalyst layer composition parameters ϵ_N , $\%Pt$ and m_{Pt} and the densities of Platinum, carbon black and electrolyte are all obtained from the values reported in [17].

Table 2

Initial data used to optimize the catalyst layer

<i>Geometry</i>			
thickness GDL, [cm]	1.0×10^{-2}	thickness cat, [cm]	1.18×10^{-3}
thickness channel, [cm]	0.1	thickness rib, [cm]	0.1
<i>Operating conditions</i>			
p , [atm]	2	T , [K]	363
x_{o_2} , [-]	0.74068	x_w , [-]	0.25932
<i>Physical properties</i>			
σ_m , [$S \cdot cm^{-1}$]	0.06 (75%RH)		
σ_S^{gdl} , [$S \cdot cm^{-1}$]	279.5	σ_S^{cl} , [$S \cdot cm^{-1}$]	32.64
$D_{o_2,w}$, [$cm^2 \cdot s^{-1}$]	0.1475	$H_{o_2,N}$, [$\frac{Pa \cdot m^3}{mol}$]	3.52611×10^4
α	1	γ	1
n	4	$c_{o_2}^{ref}$, [$mol \cdot cm^{-3}$]	1.2×10^{-6}
ϵ_N , [-]	0.3	ϵ_V^{gdl}	0.8
%Pt, [-]	0.2	m_{Pt} , [$g \cdot cm^{-2}$]	3.32×10^{-4}
ρ_{Pt} , [$g \cdot cm^{-3}$]	21.5	ρ_c , [$g \cdot cm^{-3}$]	2.0
ρ_N , [$g \cdot cm^{-3}$]	2.0		

3 The Optimization Problem and Sensitivity Analysis

A good overall measure of fuel cell performance is current density at a given potential. Therefore, if the goal is to optimize fuel cell performance at a given operating point, i.e. cell voltage, it is necessary to find the optimal catalyst layer and GDL composition that produces the maximum current density. In the model described above, the catalyst layer composition is described by three design parameters: the Nafion volume fraction, ϵ_N^{cl} , the platinum loading, m_{Pt} and the mass percentage of platinum catalyst on the support carbon black, $\%Pt$. The CL solid volume fraction was obtained from the last two parameters. The GDL composition is described by the porosity or void volume fraction, ϵ_V^{gdl} . Given this parameter, the solid phase volume fraction is readily obtained from equation (4).

3.1 The optimization problem

The optimization problem is formulated as

$$\text{maximize } i(\phi_0 = dV = V_0) \quad (29a)$$

$$\text{w.r.t. } \epsilon_N^{cl}, m_{Pt}, \%Pt, \epsilon_V^{gdl} \quad (29b)$$

$$\text{subject to: } 0 < \epsilon_V < 1 \quad (29c)$$

$$0 < \epsilon_S < 1 \quad (29d)$$

$$0 < \epsilon_N < 1 \quad (29e)$$

where the constraints guarantee that the volume fraction of each one of the three phases on the catalyst layer is not negative or larger than one. Furthermore, equation (5) is always satisfied by the way the void fraction is obtained.

Table 3

Initial upper and lower bounds for the design parameters used to optimize the catalyst layer

Design variable	Upper bound	Lower bound
ϵ_N^{cl}	0.9	0.1
m_{Pt}	2×10^{-3}	1×10^{-4}
$\%Pt$	0.9	0.1
ϵ_V^{gdl}	0.9	0.1

Finally, bounds are also set on each one of the design variables. The design variable bounds are shown in Table 3. The most important bound is the upper bound for the Platinum loading, which is constrained by cost. In this case, this value is set to 2×10^{-3} which is more than two times higher than currently used platinum loadings [30]. If this upper value is increased, this might change the optimal solution. Indeed, for an upper limit of 5×10^{-3} a new optimal solution appears at $m_{Pt} = 5 \times 10^{-3}$ and $\%Pt = 0.9$, however, this represents an excessive Platinum loading.

3.2 Analytical sensitivities

In the optimization problem above, the objective function is given by the fuel cell current density at a given electrode voltage. Current density is not one of the unknowns solved for by the analysis program, rather, it is obtained during postprocessing. The current density per unit area of a fuel cell can be obtained

by integrating the volumetric current density over the volume of CL,

$$f(\mathbf{u}, \mathbf{p}) = i(x_{o_2}, \phi_S, \phi_m; m_{Pt}, \%Pt, \epsilon_N^{cl}, \epsilon_V^{gdd}) = \frac{1}{H} \int_0^H \int_0^L \nabla \cdot \mathbf{i} dx dy \quad (30)$$

where $\nabla \cdot \mathbf{i}$ is given in equation (11), H is the height of the domain and L is the width of the domain, i.e. the thickness of the CL. Furthermore, the constraint equations in the optimization problem in (29) are directly given by the analysis model. Hence, no extra computations are required to determine the constraints.

The analytical sensitivities of the objective function f , with respect to any of the design variables p_i , can be obtained using functional analysis as

$$\begin{aligned} \frac{df(\mathbf{u}, \mathbf{p})}{dp_i} &= \frac{\partial f(\mathbf{u}, \mathbf{p})}{\partial u_j} \frac{\partial u_j}{\partial p_i} + \frac{\partial f(\mathbf{u}, \mathbf{p})}{\partial p_i} \\ &= \frac{1}{H} \int_0^H \int_0^L \left(\frac{\partial(\nabla \cdot \mathbf{i})}{\partial u_j} \frac{\partial u_j}{\partial p_i} + \frac{\partial(\nabla \cdot \mathbf{i})}{\partial p_i} \right) dx dy \quad (31) \end{aligned}$$

where \mathbf{u} is the vector of unknowns solved for by the analysis program, \mathbf{p} is the vector of design parameters, $i = 1, \dots, 3$, $j = 1, \dots, 4$, $\frac{\partial(\nabla \cdot \mathbf{i})}{\partial u_j}$ and $\frac{\partial(\nabla \cdot \mathbf{i})}{\partial p_i}$ are obtained by analytical differentiation of equation (11) with respect to the solution vector and the design variables respectively and, finally, the term $\frac{\partial u_j}{\partial p_i}$ is unknown and represents the change of the solution vector with respect to the design variables. This vector can be obtained by noticing that the residual of the governing equations has to be zero at the solution and that any perturbation in the parameters of the system should result in no variation on the residual if the residual is to be satisfied. Therefore, the total derivative of the residual has to be zero. Then, $\frac{\partial u_j}{\partial p_i}$ is computed by solving the system of partial differential equations given by

$$\frac{\partial R(\mathbf{u}, \mathbf{p})}{\partial u_j} \frac{\partial u_j}{\partial p_i} = - \frac{\partial R(\mathbf{u}, \mathbf{p})}{\partial p_i} \quad (32)$$

where $\frac{\partial R(\mathbf{u}, \mathbf{p})}{\partial u_j} \frac{\partial u_j}{\partial p_i}$ and $\frac{\partial R(\mathbf{u}, \mathbf{p})}{\partial p_i}$ represent the derivatives of the governing equations in (1) with respect to the solution vector and the design variables respectively. These are obtained using functional analysis. Note that $\frac{\partial R(\mathbf{u}, \mathbf{p})}{\partial u_j} \frac{\partial u_j}{\partial p_i}$ is a directional derivative and therefore results in a differential equation with the vector $\frac{\partial u_j}{\partial p_i}$ as the unknown [31,32]. Once an analytical expression for these terms is obtained, the system of PDEs is discretized using the finite element method with appropriate boundary conditions. In this case, the boundary conditions for the unknown vector $\frac{\partial u_j}{\partial p_i}$ are Newmann boundary conditions with value set to zero. After discretization and application of the boundary condition, the resulting linear system is solved using the GMRES method with an ILU preconditioner. The terms $\frac{\partial R(\mathbf{u}, \mathbf{p})}{\partial u_j}$ and $\frac{\partial R(\mathbf{u}, \mathbf{p})}{\partial p_i}$ depend on the solution of the governing equations and therefore this system of equations can only be solved after solving the governing equations as shown in figure 3. Finally, note that this system has the same size than the original linearized system of governing equations and that it needs to be solved for each design variable p_i . This method of obtaining the analytical sensitivities is the so-called direct formulation chosen here instead of the adjoint formulation because of its ease of implementation. A similar approach to compute sensitivities was also used in reference [33] to solve a least squares problem to estimate fuel cell model parameters from experimental data. As the number of design variables increases the adjoint formulation is proven to become more efficient [34].

Once the analytical sensitivities were implemented in the code, they were validated by comparing them to the numerical sensitivities computed using forward differences. Table 4 shows the results from the validations, performed using the data from Table 2 and with $dV = 0.3V$. The calculations were performed using adaptive mesh refinement until the change in the computed

current density between two consecutive grid refinements was less than 1%. In most cases, the final grid had 1,665 degrees of freedom, i.e. 555 nodal points. Furthermore, to ensure that the results were grid independent, the current density was also computed until the error was less than 0.1% between two consecutive grid refinements (this involved solving the problem with a grid consisting of 10,908 dof) and the difference between the two current densities was of less than 0.4%. Furthermore, the difference in all components of the gradient was less than 2%. It is important to mention that the number of degrees of freedom in the final grid is not specified and depends only on the successive refinement and coarsening to achieve the desired accuracy on the current density. The solution method used to solve the equations is discussed more comprehensively in section 3.3.

Table 4 shows good agreement between analytical and numerical sensitivities. Furthermore, this table also shows the well known problem of using numerical sensitivities, i.e. the dependence of numerical sensitivities on the step size. In this case, we observe that the numerical gradients of all variables are dependent on the step size and that gradients are only accurate for step sizes in the range 10^{-5} - 10^{-10} . It is also noticed that the optimal step size is dependent on the design variables. For ϵ_N , $\%Pt$ and ϵ_V^{ddl} the optimal step size is around $10^{-7} - 10^{-8}$ but for m_{Pt} the optimal step size is around 10^{-10} . This is most likely due to the value of the design variable being smaller. In any case, this demonstrates the clear advantage of relying on analytic sensitivities.

Table 4

Analytical vs numerical sensitivities

Design	Analytical	Numerical	Numerical	Numerical
variable		$(\delta h = 10^{-5})$	$(\delta h = 10^{-6})$	$(\delta h = 10^{-7})$
ϵ_N^cl	4.86120×10^{-1}	4.86110×10^{-1}	4.86119×10^{-1}	4.86120×10^{-1}
m_{Pt}	8.09674×10^2	7.91303×10^2	8.08947×10^2	8.09602×10^2
$\%Pt$	-5.47604×10^{-1}	-5.47615×10^{-1}	-5.47605×10^{-1}	-5.47604×10^{-1}
ϵ_V^{gdl}	-4.87682×10^{-2}	-4.87713×10^{-2}	-4.87684×10^{-2}	-4.87682×10^{-2}
Design	Numerical	Numerical	Numerical	Numerical
variable	$(\delta h = 10^{-8})$	$(\delta h = 10^{-9})$	$(\delta h = 10^{-10})$	$(\delta h = 10^{-12})$
ϵ_N^cl	4.86120×10^{-1}	4.86123×10^{-1}	4.86153×10^{-1}	4.94588×10^{-1}
m_{Pt}	8.09667×10^2	8.09673×10^2	8.09674×10^2	8.09682×10^2
$\%Pt$	-5.47604×10^{-1}	-5.47603×10^{-1}	-5.47501×10^{-1}	-5.50516×10^{-1}
ϵ_V^{gdl}	-4.87678×10^{-2}	-4.87639×10^{-2}	-4.87155×10^{-2}	-4.27445×10^{-2}

3.3 Implementation of the optimization program

The electrode finite element model together with the analytical sensitivities of the objective function and constraints are coupled to an optimization package (DOT [35]), as shown in Figure 3. In this figure, the three main iterative loops can be identified. The inner loop, the analysis loop, is used to solve the nonlinear governing equations. The middle loop, the adaptive refinement loop, is used to check the accuracy of the solution and adapt the computational

mesh as necessary using an a-posteriori error estimator. The outer loop, the optimization loop, is used to change the design parameters in order to obtain an improved design. The analysis loop starts by solving the system of nonlinear

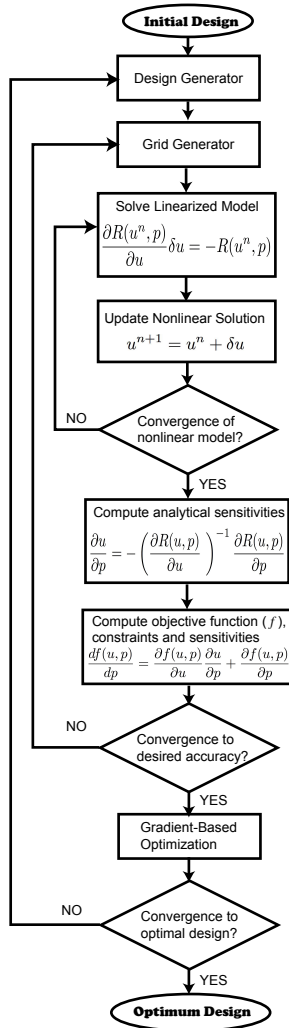


Fig. 3. Implementation of the multivariable optimization framework with adaptive refinement and analytical sensitivities

PDEs in (1) on the coarsest grid using Newton's method [36]. This method yields a quadratic rate of convergence if the initial estimate is sufficiently close to the solution and therefore, provides an efficient method to solve the system. In this case, the initial guess of the solution is constant field for each variable.

At each Newton iteration, a linearization of the system of equations given in (1)

$$\frac{\partial R_i(\mathbf{u}, \mathbf{p})}{\partial u_j} \delta u_j = -R_i(\mathbf{u}, \mathbf{p}) \quad (33)$$

is solved to obtain a solution update, $\delta \mathbf{u} = \{\delta x_{o_2}, \delta \phi_m, \delta \phi_S\}^T$. Once this system is solved, the initial solution is updated using $\mathbf{u}^{n+1} = \mathbf{u}^n + \delta \mathbf{u}$. This process is repeated until the solution satisfies the nonlinear governing equations and the update becomes nil. The convergence criteria for the Newton loop is

$$\frac{\|\mathbf{u}^{n+1} - \mathbf{u}^n\|}{\|\mathbf{u}\|} \leq 10^{-8}. \quad (34)$$

where the residual $R(\mathbf{u}, \mathbf{p})$ is also evaluated after convergence to guarantee that a true solution is obtained.

The system of equations in (33) is still a linear PDE and therefore a method to solve PDEs is necessary. In order to solve this PDE, the finite element method is used. The system is discretized using a Galerkin formulation and first order Lagrange finite elements [37]. After discretization, the system of equations yields a non-symmetric linear system of equations. This linear system is solved using an iterative solver. In particular, the generalized method of minimum residuals (GMRES) is used in conjunction with an incomplete LU decomposition (ILU) preconditioner [24,38]. Using this solver and the preconditioner, the linear system is solved at each iteration until the residual is smaller than 10^{-10} . The solution of this linear system provides the update of the solution for the next step.

The adaptive refinement loop is used in order to refine the mesh automatically during the solution process where the largest numerical errors are predicted. This allows the solver to provide always a grid independent solution even though the design parameters and therefore, the physics of the problem are

changing. Furthermore, because refinement occurs only where the errors are largest, grid adaptivity reduces computational cost by refining the grid only where necessary.

In the adaptive refinement loop, the error estimator in each cell used to decide which areas must be refined is obtained using the a posteriori error estimator developed by Kelly et al. in [39]

$$\eta_K^2 = \frac{h}{24} \int_{\partial K} \left[a_h(\mathbf{x}) \frac{\partial u_h}{\partial n} \right] dA \quad (35)$$

and implemented in deal.ii [24]. In this case, ∂K is the cell boundary, n is the normal to the cell, u_h the components of the solution, and a_h the coefficient of the original equation, in this case, $\{nFc_{total}D_{o_2}^{eff}, \sigma_m^{eff}, \sigma_S^{eff}\}$. The error estimator is computed for each cell at each adaptive refinement and the 30% of cells with the highest error are refined by dividing them into four cells while the 3% of cell with the smallest error estimation are coarsened by merging four neighboring cells. This loop is terminated when a grid independent solution is achieved. In this case, adaptive refinement is stopped when the change on the electrode current density as computed in equation (30) does not change by more than 1% in two consecutive iterations.

Finally, at the optimization loop, once the objective function, constraints and their analytical sensitivities are computed, these values are passed on to the optimization algorithms implemented in DOT, which in this case can either be a sequential quadratic programming, sequential linear programming or the modified method of feasible directions [10,35]. The optimization algorithm uses the objective function, constraints and their gradients or sensitivities to change the design parameters to achieve better performance. These parameters are passed back to the model and the process is repeated starting at the analysis

loop. Convergence of the optimization algorithm is achieved if either

$$\frac{f(\mathbf{u}, \mathbf{p}_{k+1}) - f(\mathbf{u}, \mathbf{p}_k)}{f(\mathbf{u}, \mathbf{p}_k)} \leq 10^{-6} \quad (36)$$

in four consecutive iterations or

$$\mathbf{d}_i \leq 0.0001 \quad \forall i = 1, \dots, n \quad (37)$$

Finally, to avoid runaway processes, an upper limit of 250 iterations was set. In the equations above, $f(\mathbf{u}, \mathbf{p}_i)$ represents the objective function at optimization iteration i and \mathbf{d}_i is the change on the design variable i at the current optimization iteration.

The optimization framework described was implemented using the C++ programming language and the results are discussed next.

4 Optimization Results

In order to obtain an optimal cathode electrode design, the prescription of an initial design is required to begin the optimization process. In this case, the initial input parameters used for optimization are provided in Table 2, and the optimization is performed for a voltage drop of 0.3V at the electrode. For this potential drop, an initial cell current density of $0.380784 A/cm^2$ was obtained and the non-dimensinal gradient of the current density with respect to the four optimization parameters was $\nabla_p i = \{0.145836, 0.268812, -0.109521, -0.039015\}$. The non-dimensinal gradient is used to better compare the relative sensitivity of the parameters because of the different magnitude of some of the design parameters. The non-dimensional gradient is obtained by multiplying each component by the value of the parameter at the point where the

derivative was computed, for example

$$\left. \frac{di}{dm_{Pt}} \right|_{Non-dimensional} = \left. \frac{di}{dm_{Pt}} \right|_{Dimensional} m_{Pt} \quad (38)$$

Figure 4 shows the initial and final grid after adaptive refinement. Figure 5 shows contour plots of oxygen molar fraction and solid phase potential in the GDL and Figure 6 shows contour plots of oxygen molar fraction, solid and electrolyte potentials and volumetric current densities at the cathode catalyst layer for the non-optimized cell.

The optimization problems presented in sections 4.1 and 4.2 were all solved using the three optimization algorithms: the modified method of feasible directions, the sequential linear programming and the sequential quadratic programming algorithms described in [10,35]. The modified method of feasible directions (MMFD) proved to be the most robust algorithm and gave the most accurate solution in all cases. The sequential quadratic programming algorithm was not sufficiently robust, and in most cases it stopped prematurely. The sequential linear programming algorithm proved to be more robust, but this algorithm was the most expensive computationally and it reached the maximum number of iterations in all cases. The optimization results reported in this section were thus preformed using the MMFD.

4.1 Catalyst layer optimization

In this section, the optimization problem in equation (29) was solved for the catalyst layer parameters only, i.e. only with ϵ_N^d , m_{Pt} and $\%Pt$ as design variables. The data used for the optimization problem is the data given in Table 2. Furthermore, the initial value of the design variables is set to the values

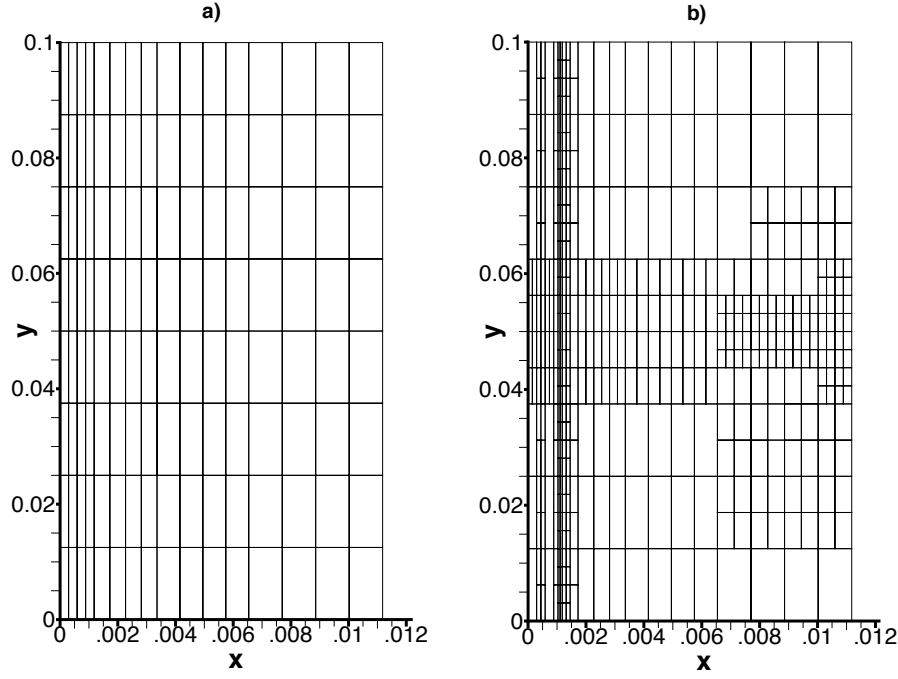


Fig. 4. Mesh used to solve the cathode electrode for the initial set of parameters. a) initial mesh, b) mesh after adaptive refinement

given in Table 2 and the GDL porosity is kept constant during optimization and it is also set equal to the value in Table 2.

The optimization problem was solved on a single AMD Opteron 64-bit CPU and a converged optimal solution obtained after 11 minutes. To achieve the optimum solution, the optimization algorithm needed 58 iterations and 239 function evaluations. Figure 7 shows the evolution of the objective function as well as the evolution of each of the design variables. The algorithm approaches the optimum solution very quickly in the first few iterations, but then it takes a relatively large number of iterations before achieving full convergence. This is due to the nonlinearity of the objective function as well as a strict convergence criteria imposed in order to guarantee that the gradient of the solution is close to zero. Figure 8 illustrates the nonlinearity of the objective function by

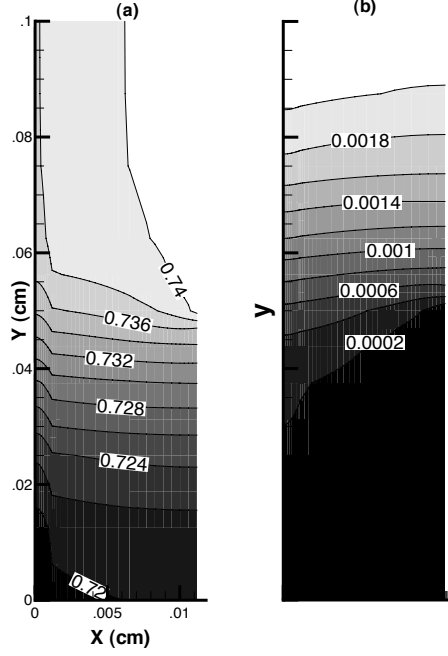


Fig. 5. Contour lines for the initial gas diffusion layer at $dV = 0.3V$ for (a) oxygen molar fraction [-], (b) potential in the solid phase [V]

plotting the design space around the optimal solution for ϵ_N^{cl} and m_{Pt} and with $\%Pt$ fixed at the optimum solution. The objective function has a banana like shape with steep gradients in one direction but smaller ones in the other. This type of function is known to be problematic for optimization algorithms [10].

At the end of the optimization, an optimum catalyst layer design is achieved that has all design variables inside the bounds specified in Table 3 and that satisfies all specified constraints. Furthermore, the non-dimensional gradient of the objective function is $\nabla_p i = \{-1.1195e - 03, -9.9265e - 04, 2.3270e - 03\}$. This value is two orders of magnitude smaller than the original gradient and it is close to zero confirming that the solution is an optimal solution.

Gradient-based optimization algorithms ensure a local optimum, but do not guarantee a global one. To verify that the optimized catalyst layer corresponds

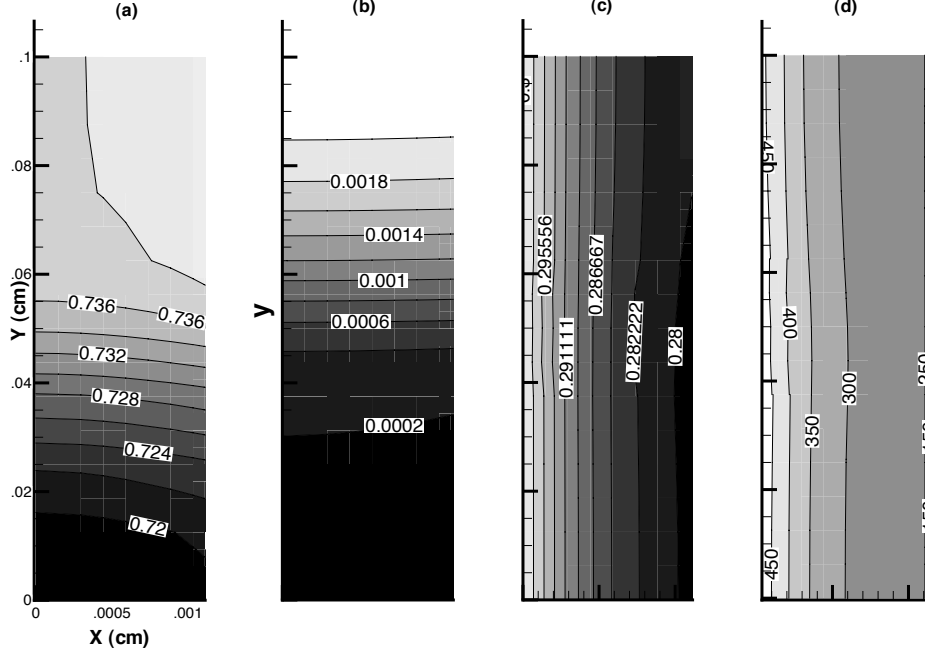


Fig. 6. Contour lines for the initial catalyst layer at $dV = 0.3V$ for (a) oxygen molar fraction [-], (b) potential in the solid phase [V], (c) potential in the electrolyte [V] and (d) volumetric current density [A/cm^3]

to a global optimum, several initial points were used to start the optimization process. Representative solutions obtained starting from two other initial designs are discussed here: $\mathbf{p}_1 = \{\epsilon_N^d, m_{Pt}, \%Pt\} = \{0.75, 10^{-3}, 0.8\}$ and $\mathbf{p}_2 = \{0.1, 10^{-4}, 0.8\}$. In both cases, the same solution was obtained as shown in Table 5. This indicates that the solution is most likely a global solution. Finally, several parametric studies such as the one shown in figure 8 with varying size domains were also performed. These studies also suggest a uni-modal objective function. Compared to the initial catalyst layer design, the optimal design yields over 50% increase in current density from $0.380784 A/cm^2$ to $0.575431 A/cm^2$. This increase is a result of a reduction in the void volume fraction from 0.12420 to 0.024602, and of the increase in both platinum load-

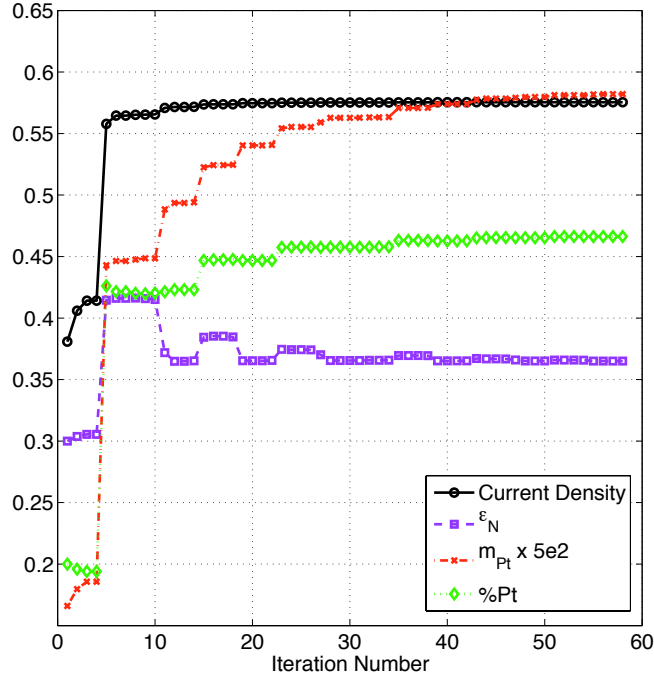


Fig. 7. Optimization history for the catalyst layer optimization process using MMFD

Table 5

Optimal catalyst layer obtained using the three different initial designs

Initial design	i	ϵ_N^{cl}	m_{Pt}	%Pt
\mathbf{p}_0	0.575431	0.365298	1.16508×10^{-3}	0.466677
\mathbf{p}_1	0.575432	0.364891	1.16641×10^{-3}	0.466806
\mathbf{p}_2	0.575432	0.364800	1.16876×10^{-3}	0.467319

ing and Nafion content. An optimal volume fraction of Nafion of 0.365298, i.e. 25.39 %wt. is in accordance with previous numerical [17] and experimental work [40]. Sasikumar et al. [40] showed experimentally that using an electrode with 20% Pt/C catalyst supports and a platinum loading of $0.5mg/cm^2$ and $0.25mg/cm^2$ the optimal Nafion content was 20% and 40% respectively. To

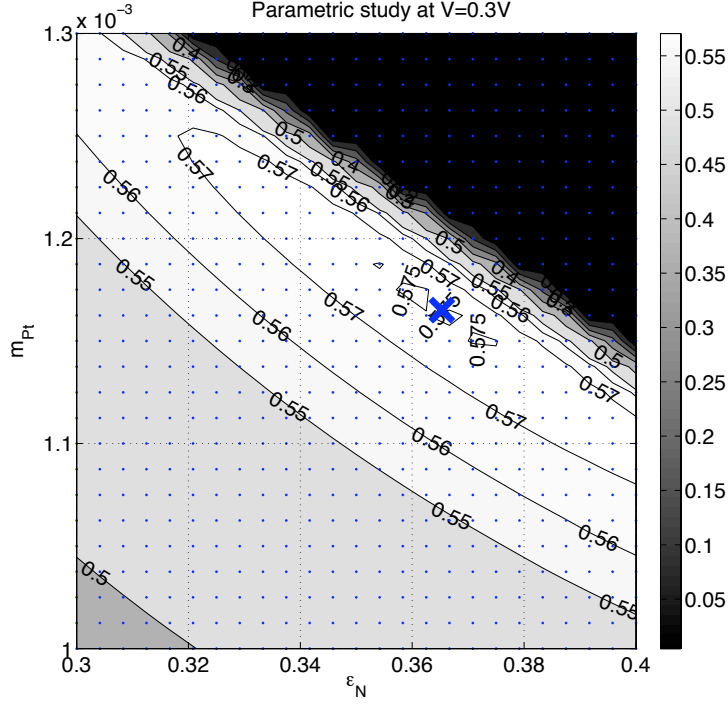


Fig. 8. Two-dimensional visualization of the objective function near the optimum solution with respect to ϵ_N^{cl} and m_{Pt} . %Pt is set to the optimum value 0.467. The cross marks the optimal design point

further validate the results, optimization was performed setting the catalyst supports to 20% Pt/C, and optimization was performed for only m_{Pt} and ϵ_N^{cl} . The results show an optimum value of $\{\epsilon_N^{cl}, m_{Pt}\} = \{0.336196, 3.70137e - 4\}$ which is equivalent to a 31.463 %wt. of Nafion and $0.370137mg/cm^2$ of platinum, which is again consistent with the experimental results by Sasikumar et al. [40]. In this case, because the optimization problem only involves two design variables the current density increases only by 11% to $0.423415A/cm^2$, therefore, illustrating the benefits of multi-parameter optimization.

Figure 9 shows the oxygen molar fraction and the potential in the solid phase of the electrode at the GDL for the optimal electrode. The oxygen distribution

pattern remains similar (cf. Fig 5) but the molar fractions are smaller consistent with the increase in current density. The solid potential distribution is also similar with changes only in the y direction, and again, an increase in the potential associated with the increase in current density.

Figure 10 shows oxygen molar fraction, solid and electrolyte potentials and volumetric current density for the optimal catalyst layer. Compared to the initial design, we note that even though the void fraction has been reduced substantially in this layer, i.e. from 0.1 to 0.025, the oxygen molar fraction is sufficient for the reaction everywhere. However, the oxygen distribution is changed substantially from an essentially one-dimensional distribution (in the y direction) in the initial design to a more complex two-dimensional distribution particularly under the current collector and area.

The solid and electrolyte phase potentials show a similar behaviour to the one shown by the initial design with the solid phase changing in the y direction and the electrolyte changing mainly in the x direction. However, in both cases, even though both electrolyte and solid phase potentials have increased, the gradients in these layers increase due to the higher current density. Finally, the volumetric current density increases substantially everywhere in the catalyst layer. However, this increase is not even and is higher near the membrane interface, resulting in larger gradients of the volumetric current density in the x direction.

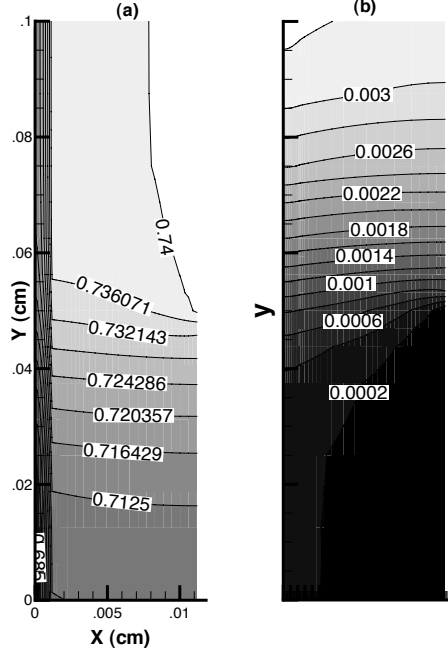


Fig. 9. Contour lines at the electrode for the optimal (MMDF) catalyst layer at $dV = 0.3V$ for (a) oxygen molar fraction [-], (b) potential in the solid phase [V]

4.2 Catalyst layer and gas diffusion layer optimization

In the preceding case, we considered optimization of the CL only. We now consider the simultaneous optimization of both CL and GDL. In particular, the optimization problem in equation (29) is solved for the catalyst layer parameters, i.e. ϵ_N^{cl} , m_{Pt} and $\%Pt$, and the gas diffusion layer parameter, ϵ_V^{gdl} . The data used for the optimization problem is the data given in 2.

The optimal solution problem is obtained in 10 minutes in a single AMD Opteron 64-bit CPU after 43 iterations and 185 function evaluations. It is interesting to note that the number of iterations is lower than in the previous case even though a new design variable has been added. Figure 11 shows the evolution of the objective function as well as the evolution of each of the design

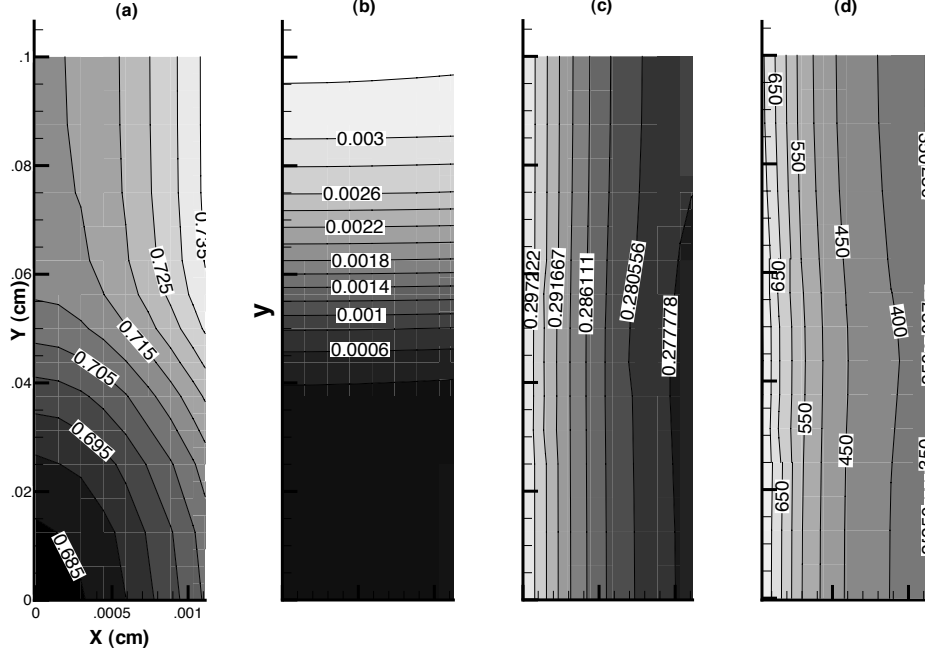


Fig. 10. Contour lines at the catalyst layer for the optimal (MMDF) catalyst layer at $dV = 0.3V$ for (a) oxygen molar fraction [-], (b) potential in the solid phase [V], (c) potential in the electrolyte [V] and (d) volumetric current density [A/cm^3]

variables. The catalyst layer design variables reach a similar solution to the previous case and the GDL porosity is reduced from 80% to approximately 60%. At the optimum electrode design, the current density is $0.582825 A/cm^2$ which represents a substantial increase with respect to the original current density $0.380784 A/cm^2$ but only a slight increase with respect to the catalyst layer optimum design, $0.575431 A/cm^2$. The gradient of the objective function in the optimal solution is small, $\nabla_p i = \{3.5533e - 03, 4.1798e - 03, -5.9847e - 03, -1.3133e - 03\}$ again demonstrating that the solution is indeed an optimal solution consistent with all constraints. As in the previous section, to check that the solution is a global optimum, the problem was solved starting from 2 additional initial designs: $\mathbf{p}_1 = \{\epsilon_N^{cl}, m_{Pt}, \%Pt, \epsilon_V^{gdl}\} = \{0.75, 10^{-3}, 0.8, 0.2\}$

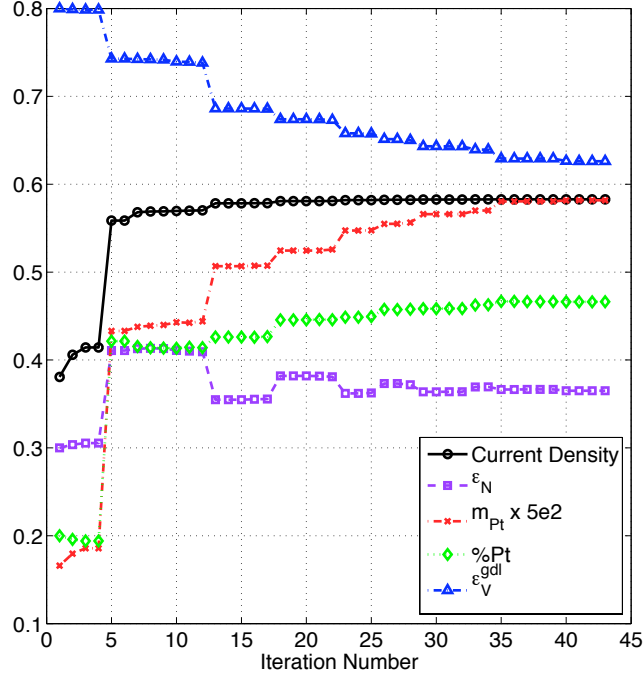


Fig. 11. Optimization history plot for the catalyst layer and GDL optimization process using MMFD and $\mathbf{p}_2 = \{0.1, 10^{-4}, 0.8, 0.5\}$. The solutions are listed in Table 2 are shown in Table 6. As in the previous case, the same solution is obtained from all three initial designs with only negligible differences that could be further reduced by using a more stringent convergence criteria. A comparison of the solution Table 6

Optimal catalyst layer obtained using the three different initial designs

Initial design	i	ϵ_N^{cl}	m_{Pt}	%Pt	ϵ_V^{gdl}
\mathbf{p}_0	0.582825	0.365057	1.16335×10^{-3}	0.466330	0.626133
\mathbf{p}_1	0.582831	0.364898	1.16534×10^{-3}	0.466650	0.614249
\mathbf{p}_2	0.582731	0.364538	1.18691×10^{-3}	0.471506	0.597430

from the catalyst layer optimization in Table 5 and the solution from the elec-

trode optimization in Table 6 shows that the catalyst layer design variables remain almost unchanged when the GDL porosity is introduced into the optimization, while the GDL porosity is reduced from 80% to 60%. The relatively small improvement in current density by adding the GDL design parameter into the optimization and the small changes in catalyst layer composition are not unexpected in this case because the reaction in the CL is not transport limited. This makes the coupling between the GDL and the catalyst layer less important and, therefore, not much improvement is achieved by adding the GDL parameter into the optimization process.

Figure 12 shows the oxygen molar fraction and solid phase potential at the optimum electrode. Because the porosity is decreased, the potential at the solid phase is reduced, reducing also voltage losses at the GDL. Meanwhile, the mass transfer is also slightly decreased, however, this does not affect substantially the reaction because there is always sufficient oxygen for the reaction. Figure 13 shows the effects of the GDL optimization on the catalyst oxygen molar fraction, solid and electrolyte phases and reaction rate. The effect is similar to that in the GDL. Because of the drop in the oxygen molar fraction in the GDL, the oxygen molar fraction is also slightly reduced at the catalyst layer. Similarly, the decrease in solid potential at the GDL results in a reduction of the solid potential in the catalyst layer. This last value increases the overpotential at the CL which in turn increases the volumetric current density slightly. This increase is larger under the gas channel where the solid potential has been reduced the most. Finally, the electrolyte potential remains almost constant, with a small increase due to the higher current density.

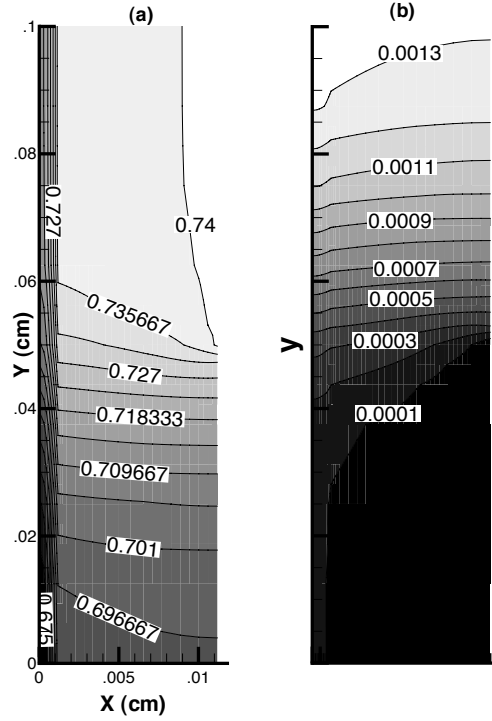


Fig. 12. Contour lines at the electrode for the optimal (MMDF) electrode at $dV = 0.3V$ for (a) oxygen molar fraction [-], (b) potential in the solid phase [V]

4.3 Overall performance of the optimized cathode electrode

The optimization of the cathode electrode has been performed at a given voltage drop of $0.3V$. There is not a guarantee that the performance improvements obtained by optimizing the design at this overpotential will also be achieved over the entire polarization curve. To conclude the study, the polarization curves corresponding to the initial and optimal designs are plotted in Figure 14. Only low to intermediate currents are considered since two-phase flow is not taken into account in this model and the effect of liquid water saturation can become important at high current densities [3]. For an overpotential of $0.3V$ at which the optimization was performed, the water molar fraction

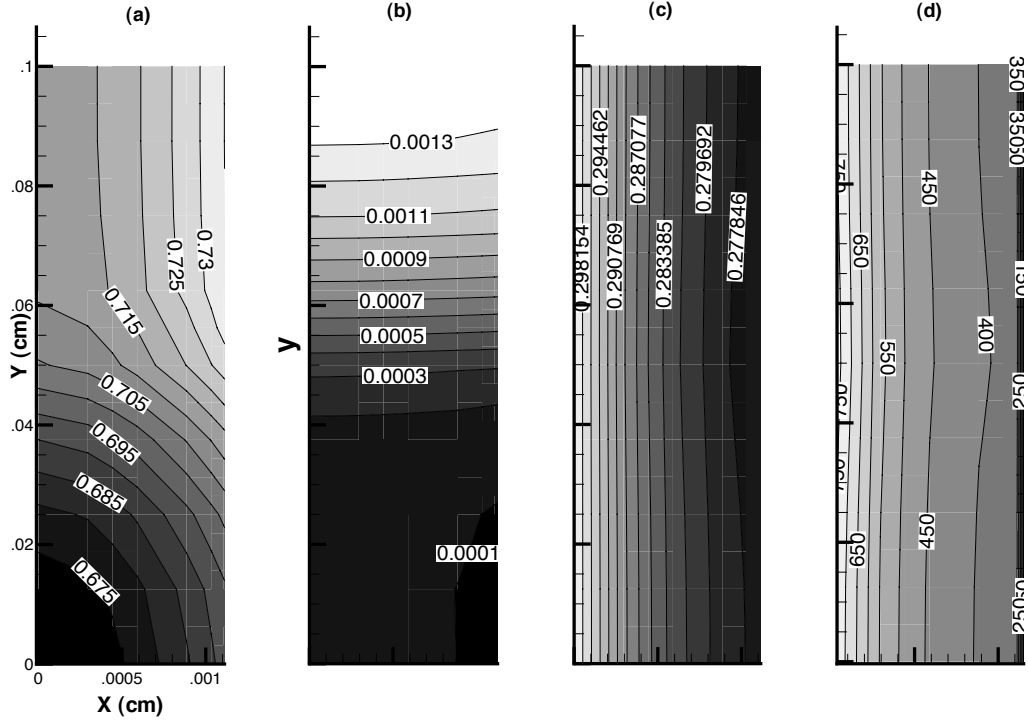


Fig. 13. Contour lines at the catalyst layer for the optimal (MMDF) electrode at $dV = 0.3V$ for (a) oxygen molar fraction [-], (b) potential in the solid phase [V], (c) potential in the electrolyte [V] and (d) volumetric current density [A/cm^3]

reaches a maximum value of 0.325 under the current collector at the membrane/catalyst layer interface. This value is close to the value of 0.346 at which saturation can occur at the cell operating conditions. The polarization curve of the improved design shows indeed an improvement over the initial design over the entire range of pertinent current densities, and not only at the given design voltage of 0.3V.

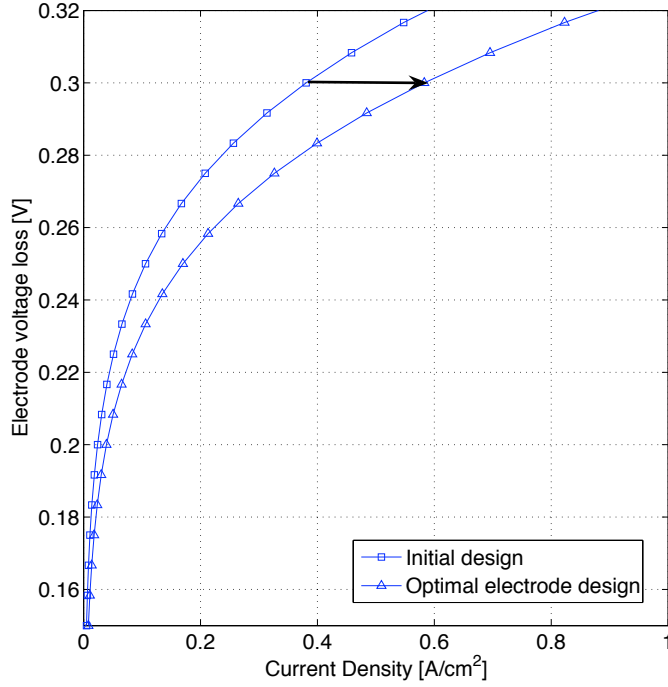


Fig. 14. I-V plot for the initial and optimum cathode electrode design

5 Conclusions

In this paper, a numerical optimization framework able to perform systematic PEM fuel cell cathode design has been presented. In order to develop the framework, a gradient-based optimization algorithm has been coupled with a two-dimensional PEM fuel cell cathode model. This framework represents the first documented attempt to perform numerical optimization of a cathode electrode using a two-dimensional model. The model is used to compute electrode current density and its analytical sensitivities with respect to cathode design parameters. The electrode current density is then used as the objective of the cathode optimization problem.

In order to achieve the maximum current density, the framework was used to obtain the optimum CL and GDL compositions. Optimization results show

that, by optimizing the catalyst layer composition, the current density can be increased by more than 50%. This increase is due to a substantial reduction in porosity, from 0.12420 to 0.024602, and an increase of both platinum mass loading and ionomer volume fraction. In order to ensure that there is enough porosity in the catalyst layer and, at the same time, to be able to increase platinum loading to the desired amount, the percentage of platinum per carbon black is increased with respect to the initial design. Another finding of note is that, at low current densities when mass transport is not limiting, introducing the gas diffusion layer composition to the optimization problem does not significantly affect the optimal catalyst layer design, and only small improvements in fuel cell performance are obtained.

The optimization results also demonstrate that this framework is capable of producing optimal cathode compositions using only a small amount of computational resources; less than 15 minutes of computational time on a single processor. This computational efficiency is due to the use of Newton’s method to solve the nonlinear governing equations and the use of analytical sensitivities during optimization. The cathode model presented in this paper is restricted to two-dimensions; however, results suggest that the same numerical optimization methodology could be extended to perform three-dimensional multi-parameter fuel cell optimization also requiring only a reasonable amount of computational resources.

6 Acknowledgments

Financial support from the Natural Sciences and Engineering Research Council of Canada and the Canada Research Chair Program are gratefully acknowl-

edged.

Nomenclature

$\%Pt$	mass percentage of platinum catalyst on the support carbon black
α	transfer coefficient [-]
ϵ_V^{cl}	void volume fraction in the catalyst layer [-]
ϵ_V^{gdl}	void volume fraction in the GDL [-]
ϵ_N^{cl}	Nafion volume fraction in the catalyst layer [-]
ϵ_S^{cl}	solid phase volume fraction in the catalyst layer [-]
ϵ_V^{cl}	void volume fraction in the catalyst layer [-]
ϵ_S^{gdl}	solid phase volume fraction in the GDL [-]
γ	coefficient in Tafel equation [-]
$\hat{H}_{O_2,w}$	Henry's law coefficient for the oxygen in Nafion [$\frac{Pa \cdot m^3}{mol}$]
ϕ_m	membrane potential [V]
ϕ_s	solid phase potential [V]
ρ_c	Carbon density [$g \cdot cm^{-3}$]
ρ_{Pt}	Platinum density [$g \cdot cm^{-3}$]
$\sigma_m^{eff-gdl}$	effective electrolyte conductivity in the GDL [$S \cdot cm^{-1}$]
$\sigma_S^{eff-gdl}$	effective solid phase conductivity in the GDL [$S \cdot cm^{-1}$]
σ_m^{eff-cl}	effective electrolyte conductivity in the catalyst layer [$S \cdot cm^{-1}$]
σ_S^{eff-cl}	effective solid phase conductivity in the catalyst layer [$S \cdot cm^{-1}$]
σ_m^{eff}	effective electrolyte conductivity in either the GDL or the CL [$S \cdot cm^{-1}$]
σ_S^{eff}	effective solid phase conductivity in either the GDL or the CL [$S \cdot cm^{-1}$]
A_0	catalyst surface area per unit mass of the catalyst particles [cm^2/g]
A_v	specific reaction surface area per volume of catalyst layer [$1/cm$]
$c_{O_2}^{Nafion}$	concentration of oxygen dissolved in the Nafion [$mol \cdot cm^{-3}$]

$c_{o_2}^{ref}$	concentration of oxygen [$mol \cdot cm^{-3}$]
c_{total}	concentration of the binary mixture of oxygen and water vapour [$mol \cdot cm^{-3}$]
$D_{o_2}^{eff}$	effective diffusion coefficient in either the GDL or the CL [$cm^2 \cdot s^{-1}$]
$D_{o_2,w}$	oxygen diffusion coefficient in water vapour [$cm^2 \cdot s^{-1}$]
$D_{o_2}^{eff-cl}$	effective oxygen diffusion coefficient in the catalyst layer [$cm^2 \cdot s^{-1}$]
$D_{o_2}^{eff-gdl}$	effective oxygen diffusion coefficient in the GDL [$cm^2 \cdot s^{-1}$]
dV	applied voltage to the electrolyte [V]
F	Faraday constant, 96493 [$C \cdot mol$]
i	current density, [A/cm^{-2}]
i_0^{ref}	exchange current density, [A/cm^{-2}]
L	length of the catalyst layer [cm]
m_{Pt}	catalyst platinum mass loading per unit area on the catalyst [$g \cdot cm^{-2}$]
n	electrons produced in the cathodic reaction
p	pressure of the binary mixture [Pa]
p_{o_2}	oxygen partial pressure [Pa]
R	gas constant, 8.315 [$J \cdot K^{-1} \cdot mol^{-1}$]
T	temperature [K]
x_{o_2}	oxygen molar fraction [-]

References

- [1] A. Z. Weber, J. Newman, Modeling transport in polymer-electrolyte fuel cells, Chemical Reviews 104 (10) (2004) 4679–4726.
- [2] T. Berning, N. Djilali, Three-dimensional computational analysis of transport phenomena in a pem fuel cell - a parametric study, Journal of Power Sources

124 (2) (2003) 440–452.

- [3] T. Berning, N. Djilali, A 3d, multiphase, multicomponent model of the cathode and anode of a PEM fuel cell, *Journal of the Electrochemical Society* 150 (12) (2003) A1589–A1598.
- [4] P. Sui, N. Djilali, Analysis of coupled electron and mass transport in the gas diffusion layer of a pem fuel cell, *Journal of Power Sources* (2006) In press.
- [5] J.G.Pharoah, D. Harvey, K. Karan, Comparision of catalyst treatements for PEM fuel cell modelling, in: 4th ASME Conference on Fuel Cell Science, Engineering and Technology, Irvine, California, 2006.
- [6] P. Sui, S. Kumar, N. Djilali, Design and optimization of the gas channels of a pemfc using cfd-based simulation tools, in: 4th ASME Conference on Fuel Cell Science, Engineering and Technology, Irvine, California, 2006.
- [7] T. A. Zang, L. L. Green, Multidisciplinary design and optimization techniques: Implications and opportunitites for fluid dynamics research, in: 30th AIAA Fluid Dynamics Conference, Norfolk, VA, 1999.
- [8] J. Martins, A coupled-adjoint method for high-fidelity aero-structural optimization, Ph.D. thesis, Standford University (November 2002).
- [9] M. Secanell, A. Suleman, Numerical evaluation of optimization algorithms for low-reynolds-number aerodynamics shape optimization, *AIAA Journal* 43 (10) (2005) 2262–2267.
- [10] G. Vanderplaats, *Numerical Optimization Techniques for Engineering Design with Applications*, McGraw-Hill, 1984.
- [11] M. Eldred, D. Outka, W. Bohnhoff, W. Witkowski, V. Romero, E. Ponslet, K. Chen, Optimization of complex mechanics simulations with object-oriented software design, *Computer Modeling and Simulation in Engineering* 1 (3) (1996) 323–352.

- [12] A. Mawardi, F. Yang, R. Pitchumani, Optimization of the operating parameters of a proton exchange membrane fuel cell for maximum power density, *Journal of Fuel Cell Science and Technology* 2 (2) (2005) 121–135.
- [13] M. Grujicic, K. Chittajallu, Design and optimization of polymer electrolyte membrane (PEM) fuel cells, *Applied surface science* 227 (2004) 56–72.
- [14] M. Grujicic, K. Chittajallu, Optimization of the cathode geometry in the polymer electrolyte membrane (PEM) fuel cells, *Chemical Engineering Science* 59 (2004) 5883–5895.
- [15] M. Grujicic, C. Zhao, K. Chittajallu, J. Ochterbeck, Cathode and interdigitated air distributor geometry optimization in polymer electrolyte membrane (PEM) fuel cells, *Materials Science and Engineering B* 108 (2004) 241–252.
- [16] Z. Zhang, X. Wang, X. Zhang, F. Yu, Optimizing the performance of a PEM fuel cell using the powell algorithm, in: *Proceedings of the 4th International Conference on Fuel Cell Science, Engineering and Technology*, Irvine, CA, 2006.
- [17] D. Song, Q. Wang, Z. Liu, T. Navessin, M. Eikerling, S. Holdcroft, Numerical optimization study of the catalyst layer of pem fuel cell cathode, *Journal of Power Sources* 126 (1-2) (2004) 104–111.
- [18] D. Song, Q. Wang, Z. Liu, M. Eikerling, Z. Xie, T. Navessin, S. Holdcroft, A method for optimizing distributions of Nafion and Pt in cathode catalyst layers of PEM fuel cells, *Electrochimica Acta* 50 (16-17) (2005) 3359–3374.
- [19] M. Eikerling, A. Kornyshev, Modelling the performance of the cathode catalyst layer of polymer electrolyte fuel cells, *Journal of Electroanalytical Chemistry* 453 (1-2) (1998) 89–106.
- [20] A. Kulikovskiy, J. Divisek, A. Kornyshev, Modeling the cathode compartment of polymer electrolyte fuel cells: Dead and active reaction zones, *Journal of the Electrochemical Society* 146 (11) (1999) 3981–3991.

- [21] C. Marr, X. Li, Composition and performance modelling of catalyst layer in a proton exchange membrane fuel cell, *Journal of Power Sources* 77 (1) (1999) 17–27.
- [22] W. Sun, B. A. Peppley, K. Karan, An improved two-dimensional agglomerate cathode model to study the influence of catalyst layer structural parameters, *Electrochimica Acta* 50 (16-17) (2005) 3347–3358.
- [23] A. Parthasarathy, S. Srinivasan, A. J. Appleby, C. Martin, Temperature dependence of the electrode kinetics of oxygen reduction at the platinum/nafon(r) interface - a microelectrode investigation, *Journal of the Electrochemical Society* 139 (9) (1992) 2530–2537.
- [24] W. Bangerth, R. Hartmann, G. Kanschat, `deal.II` Differential Equations Analysis Library, Technical Reference.
URL <http://www.dealii.org>
- [25] L. You, H. Liu, A parametric study of the cathode catalyst layer of PEM fuel cells using a pseudo-homogeneous model, *International Journal of Hydrogen Energy* 26 (9) (2001) 991–999.
- [26] T. Springer, T. Zawodzinski, S. Gottesfeld, Polymer electrolyte fuel cell model, *Journal of the Electrochemical Society* 138 (8) (1991) 2334–2342.
- [27] M. V. Williams, E. Begg, L. Bonville, H.R.Kunz, J. Fenton, Characterization of gas diffusion layers for pemfc, *Journal of the Electrochemical Society* 151 (8) (2004) A1173–A1180.
- [28] D. Pantea, H. Darmstadt, S. Kaliaguine, C. Roy, Electrical conductivity of conductive carbon blacks: influence of surface chemistry and topology, *Applied Surface Science* 217 (1-4) (2003) 181–193.
- [29] E. L. Cussler, *Diffusion : Mass Transfer in Fluid Systems*, 2nd Edition, Cambridge University Press, 1997.

- [30] S. Litster, G. McLean, PEM fuel cell electrodes, *Journal of Power Sources* 130 (1-2) (2004) 61–76.
- [31] D. G. Luenberger, *Optimization by vector space methods*, John Wiley & Sons, New York, 1969.
- [32] K. Yosida, *Functional analysis*, Springer-Verlag, Berlin, 1965.
- [33] B. Carnes, N. Djilali, Systematic parameter estimation for PEM fuel cell models, *Journal of Power Sources* 144 (1) (2005) 83–93.
- [34] D. Cacuci, *Sensitivity and Uncertainty Analysis: Theory*, Vol. 1, Chapman and Hall/CRC, Boca Raton, Florida, USA, 2003.
- [35] Vanderplaats Research & Development, Inc., *DOT: Design Optimization Tools Users Guide*. Version 5.0 (2001).
- [36] W. H. Press, S. A. Teukolsky, W. Vetterling, B. Flannery, *Numerical Recipes in C++: The Art of Scientific Computing*, 2nd Edition, Cambridge University Press, Cambridge, 2002.
- [37] E. B. Becker, G. Carey, J. Oden, *Finite Elements: An Introduction*, Vol. 1, Prentice-Hall, Englewoods Cliffs, 1981.
- [38] R. Barrett, M. Berry, T. F. Chan, J. Demmel, J. Donato, J. Dongarra, V. Eijkhout, R. Pozo, C. Romine, H. V. der Vorst, *Templates for the Solution of Linear Systems: Building Blocks for Iterative Methods*, 2nd Edition, SIAM, Philadelphia, PA, 1994.
- [39] D. W. Kelly, J. P. de S. R. Gago, O. C. Zienkiewicz, I. Babuska, A posteriori error analysis and adaptive processes in the finite element method: Part i - error analysis, *International Journal for Numerical Methods in Engineering* 19 (11) (1983) 1593–1619.

- [40] G. Sasikumar, J. Ihm, H. Ryu, Optimum Nafion content in PEM fuel cell electrodes, *Electrochimica Acta* 50 (2-3) (2004) 601–605.